Energy Engineering

Tech Science Press

Doi:10.32604/ee.2025.074702

ARTICLE

Short-Term Solar Radiation Forecasting System for Jiangsu Province Based on FY-4A Multispectral Data-Regional Applicability Validation for High-Penetration Photovoltaic Grid Integration

Yunlong Du[1], Shuyi Zhuang[2,*], Zhigang Ye[2], Qiangsheng Bu[2], Yun Chai[1] and Yuanbing Wang[3]

[1]State Grid Jiangsu Electric Power Co., Ltd., Nanjing, 210024, China
[2]Electric Power Research Institute, State Grid Jiangsu Electric Power Co., Ltd., Nanjing, 211103, China
[3]School of Atmospheric Sciences, Nanjing University of Information Science and Technology, Nanjing, 210044, China

*Corresponding Author: Shuyi Zhuang. Email: zhuangshuyi2014@126.com

Received: 16 October 2025; Accepted: 22 December 2025; Published: 30 August 2026

ABSTRACT: Under the dual challenges of global warming and energy transition, improving the short-term forecasting accuracy of surface solar radiation is of great practical importance for photovoltaic (PV) power integration. In this study, a short-term solar radiation forecasting model based on the XGBoost machine learning algorithm was developed for Jiangsu Province by integrating multispectral data from the Fengyun-4A (FY-4A) geostationary satellite with ground-based meteorological observations. The model incorporated 18 input features—including satellite reflectance, solar zenith angle, normalized difference vegetation index (NDVI), elevation, and land-cover data—to dynamically predict ground horizontal irradiance (GHI) with 0–4 h lead times. Systematic validation using data from 17 provincial stations during 2023 demonstrated that the model achieved a root mean square error (RMSE) of 165.62 W/m^2 and a correlation coefficient (R) of 0.82 for 1-h forecasts, representing an approximately 23% reduction in RMSE compared with traditional numerical weather prediction (NWP) models. Forecast errors exhibited distinct seasonal variability, with spring and summer forecasts (RMSE: 182.76 and 184.86 W/m^2) performing significantly better than autumn (223.58 W/m^2) and winter (194.07 W/m^2), a pattern consistent with seasonal changes in cloud–aerosol interactions under the East Asian monsoon regime. Three anomalous stations with elevated RMSEs (>300 W/m^2) were further identified, primarily attributed to localized radiation attenuation over coastal wetlands, urban agglomerations, and mining surfaces. Nevertheless, correlation coefficients between predicted and observed values remained above 0.70, confirming the capability of FY-4A multispectral data to capture short-term radiation dynamics. Overall, this study establishes an innovative short-term forecasting framework suitable for the complex meteorological conditions of China's eastern coastal regions. The achieved 1-h forecasting accuracy satisfies the ≤20% relative error requirement specified in the Technical Specifications for Power Forecasting Systems of Photovoltaic Power Stations, providing robust technical support for renewable energy integration across the Yangtze River Delta.

KEYWORDS: Fengyun-4A (FY-4A); Jiangsu Province; XGBoost machine learning short-term forecasting model; dynamic prediction

1 Introduction

In recent years, climate warming has intensified, leading to frequent extreme weather events: From late June to early July 2021, the northwestern regions of the United States and Canada experienced a once-in-a-century "high-pressure heat dome" heatwave, with maximum temperatures exceeding 49.6°C in some locations, resulting in hundreds of deaths and extensive agricultural and livestock losses [1]; During the summer of 2022, Pakistan endured its worst monsoon floods on record, affecting over 33 million people and claiming nearly 1500 lives [2]; In 2023, Europe simultaneously endured the largest wildfires on record, widespread flooding during its wettest year ever, and severe marine heatwaves; In July 2024, Southeast Europe experienced its longest-ever heatwave, with 13 consecutive days of "severe heat stress" affecting 55% of the region's land area and shattering multiple local temperature records. Massive carbon dioxide emissions from human activities are the primary drivers of these anomalies [3]. Global coal-fired power plants produce approximately 3 billion tons of CO_2 annually, accounting for 45% of total global greenhouse gas emissions. Coal-fired power alone contributes over 70% of energy-related CO_2 emissions worldwide.

To curb the further intensification of the greenhouse effect, China has continuously invested in the new energy sector in pursuit of "dual carbon" goals of carbon peaking and carbon neutrality [4]. By the end of 2020, wind and solar power generation accounted for 9.8% of China's total annual electricity production. By the end of 2024, this proportion had risen to 19%. The rapid expansion of wind and solar power has introduced new demands for grid integration. In some regions, monthly curtailment rates reached as high as 42.7%, indicating that grid peak-shaving capacity still needs to be better aligned with the growth rate of installed capacity. Photovoltaic (PV) generation efficiency is significantly influenced by surface solar radiation. Improving the short-term forecasting accuracy of surface solar radiation at PV sites can not only reduce system reserve costs but also minimize curtailment. However, surface solar radiation is influenced by weather systems at various scales, exhibiting high uncertainty. Radiation forecasting at 0–4-h scales faces multiple challenges. On one hand, spatiotemporal variations in clouds and atmospheric constituents (e.g., aerosols, water vapor) cause the radiation field to exhibit high nonlinearity and randomness, posing assimilation and error correction difficulties for traditional physical models and numerical weather prediction [5]. On the other hand, China's ground-based solar radiation observation stations are sparse and unevenly distributed, particularly in eastern coastal areas and certain complex terrain regions where observational data is severely lacking. This scarcity makes it difficult to meet the high spatio-temporal resolution requirements for short-term forecasting algorithms [6].

Geostationary meteorological satellites offer extensive spatial coverage and high-frequency observation capabilities [7]. Their surface solar incident radiation products account for atmospheric components such as clouds and aerosols. By integrating these satellite data with ground-based solar radiation measurements, spatio-temporal variations in surface solar radiation can be effectively captured. Currently, in-orbit meteorological satellites capable of real-time monitoring across China include China's Fengyun-4 series, Japan's Himawari series, and South Korea's Kilsan series [8–10]. Among these, Fengyun-4 has accumulated extensive data since its 2016 launch and provides comprehensive coverage of China, offering a high-spatiotemporal-resolution data source for photovoltaic power forecasting.

Traditional surface solar radiation forecasting relies on ground observations, which suffer from site heterogeneity, making model generalization to specific regions challenging [11]. In recent years, numerous studies have emerged combining remote sensing data to retrieve and predict surface solar radiation. Wang et al. collected 18 months of irradiance data from a photovoltaic site and used 2020 observations from the Fengyun-4A satellite (FY-4A) as input features to retrieve surface irradiance. Results showed that applying the XGBoost algorithm to retrieve irradiance improved accuracy by over 5% [12]. Jia et al. focused on analyzing the impact of remote sensing data on irradiance prediction. Their study demonstrated that incorporating remote sensing data significantly improved overall prediction accuracy across different observation sites. Adding remote sensing data optimized prediction performance for various time steps and substantially reduced the probability of large prediction errors [13,14]. Nevertheless, their work did not explicitly examine the performance of satellite-based products in regions with complex monsoon-influenced radiation variability.

Overall, existing literature shows that satellite-enhanced forecasting is promising, but two major limitations persist: (1) most studies focus on retrieval accuracy rather than short-term forecasting capability, and (2) few works systematically evaluate satellite-derived radiation products under complex mesoscale weather conditions, especially in eastern coastal China. These gaps motivate the need for region-specific assessments and tailored forecasting strategies.

Jiangsu Province, situated in China's eastern monsoon region, exhibits a typical subtropical monsoon climate with distinct seasons [15]. Influenced by the East Asian monsoon circulation and urbanization, this area experiences frequent cloud cover changes (annual average cloud cover reaches 65%) and consistently high aerosol optical depth exceeding 0.8 (reaching 1.2 in the core Yangtze River Delta urban cluster), leading to significant spatiotemporal variation in solar radiation. Statistical data indicate that Jiangsu's annual average sunshine duration is 1980 h, with a north-south disparity of 300 h [16]. During spring (March–May), the complex interaction between the plum rain front and aerosols results in highly variable weather systems, causing daily irradiance fluctuations exceeding 50%, posing severe challenges to the stability of photovoltaic power generation. As a national renewable energy demonstration zone, Jiangsu's installed PV capacity has surpassed 25 GW (as of 2023), accounting for 18.7% of the province's total installed power generation capacity, with distributed PV exceeding 40% of this total. However, the coupled effects of high PV grid integration and complex meteorological conditions have dramatically increased peak-shaving pressure on the grid. During typical rainy weather, provincial PV output can plummet by 70% within an hour, urgently requiring high-precision short-term radiation forecasting technology. This paper analyzes the suitability of FY-4A-based surface solar radiation prediction products for Jiangsu Province using ground solar irradiance observation data from multiple PV power stations within the province. It explores the application effectiveness of new-generation geostationary meteorological satellite radiation inversion products in short-term radiation forecasting for eastern coastal regions.

To address these challenges, this study proposes a short-term solar radiation forecasting framework specifically designed for the monsoon-driven and highly variable atmospheric conditions of Jiangsu Province. The contributions of this work can be summarized as follows:

(1) We integrate high-temporal-resolution multispectral observations from the FY-4A geostationary satellite with ground-based meteorological data, effectively mitigating the spatial sparsity and heterogeneity of existing radiation observation networks;
(2) We develop an XGBoost-based prediction model that incorporates 18 satellite-, atmosphere-, and land-surface–derived variables, enabling dynamic forecasts of ground horizontal irradiance with 0–4-h lead times;
(3) We conduct comprehensive validation using data from 17 provincial stations, demonstrating substantial accuracy gains over traditional numerical weather prediction approaches and identifying clear seasonal and spatial error patterns, thereby providing a reliable and application-ready technical foundation for photovoltaic power integration in the eastern coastal regions of China.

2 Data and Methods

2.1 Data Sources

2.1.1 FY-4A Satellite Observation Data

China's second-generation geostationary meteorological satellite, Fengyun-4A (FY-4A), was successfully launched on 11 December 2016. The satellite carries four payloads: the Advanced Geostationary Radiation Imager (AGRI) [17–19], the Geostationary Infrared Interferometer (GIIRS), the Lightning Imager (LMI), and the Space Environment Monitoring (SEP) component. AGRI features 14 spectral bands spanning from 0.47 μm in the visible range to 13.8 μm in the infrared range. Its spatial resolution varies by band: 1 km at nadir in the visible bands, 2 km in the near-infrared bands, and 4 km in the infrared bands. Compared to the five bands of the preceding FY-2 series, this increased spectral coverage enables more effective aerosol inversion by geostationary satellites. FY-4A's high temporal resolution offers significant advantages in air quality monitoring and modeling, enhancing the detection and tracking of haze [20].

Atmospheric top-of-atmosphere (TOA) reflectance at specific wavelengths results from the combined effects of surface-reflected radiation and atmospheric scattering, excluding direct surface interactions [21]. This angular spectral reflectance is closely related to solar zenith angle (SZA) and aerosol optical properties. In remote sensing studies, SZA is critical because larger zenith angles correspond to longer atmospheric paths, amplifying scattering and absorption effects. These effects may attenuate radiation reaching the Earth's surface and alter the reflected signals detected by sensors. Within this framework, the input features for this study include reflectance data from 13 out of the 14 AGRI spectral bands, together with solar zenith angle, land-cover type, and surface elevation information [22]. The remaining AGRI band, which is primarily designed for atmospheric sounding, was excluded to reduce redundancy in the predictor set (http://satellite.nsmc.org.cn). Although the AGRI instrument provides 14 spectral bands, their physical relevance to surface solar radiation differs. The visible and near-infrared bands (Bands 1–6) exhibit the strongest correlation with ground irradiance because they directly capture reflected shortwave radiation and cloud optical properties. The mid-infrared bands (Bands 7–10) provide information on atmospheric water vapor and temperature profiles, showing moderate correlation under varying meteorological conditions. The thermal infrared bands (Bands 11–14) are mainly sensitive to land surface temperature, cloud-top height, and cloud phase, which are indirectly related to irradiance but remain essential for characterizing cloud structures—one of the dominant factors affecting short-term radiation fluctuations. Therefore, although the thermal infrared bands are less directly correlated with surface radiation, they supply complementary cloud information that improves the model's ability to predict rapid irradiance changes. Considering these physical linkages, all 13 AGRI reflectance bands were retained as predictors to ensure that the model captures cloud, aerosol, and surface heterogeneity effects comprehensively.

2.1.2 Ground Observation Data, CMA Sites

The China Meteorological Administration (CMA) provides ground radiation observation data from 162 stations across China, with their spatial distribution shown in Fig. 1. The thermoelectric total solar radiation pyranometers deployed in the CMA observation network have a spectral response range of 0.3 to 3.0 μm, with a measurement uncertainty of ±3% [23,24]. This study collected hourly horizontal total radiation observations from January to December 2023, covering the time period 00:00–09:00 (UTC) daily.

2.1.3 Ground-Based Observation Data: Stations within Jiangsu Province

Ground-based radiation observation data from 17 stations within Jiangsu Province were used in this study, and their spatial distribution is shown in Fig. 2. Unlike the CMA radiation network, which is operated under unified national standards, the Jiangsu stations are irradiance sensors installed within PV power plants and maintained by the power grid company as part of plant monitoring systems. Consequently, the instrument types, calibration procedures, mounting configurations, and exposure to local shading may differ from those at CMA sites, potentially introducing additional systematic uncertainty at the Jiangsu stations compared with the national radiation network. To match the 15-min temporal resolution of the satellite data used in this study, the 15-min horizontal total radiation observations from the Jiangsu stations were downsampled to an effective 1-h temporal resolution.

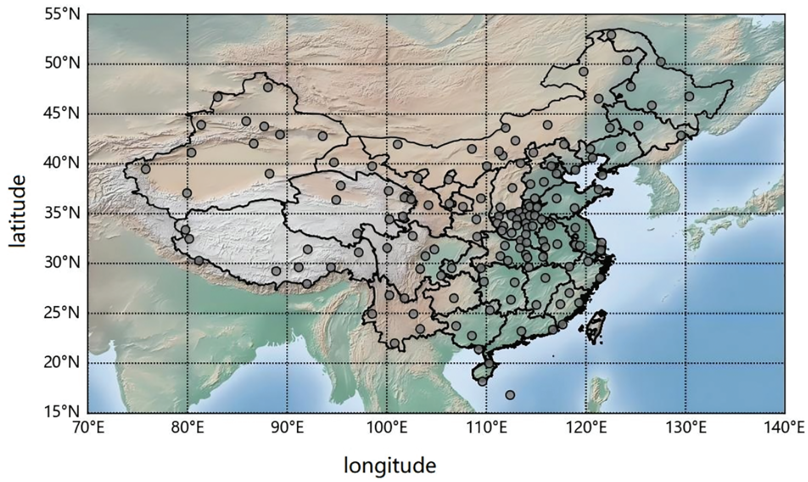

Figure 1: Distribution of regional surface solar observation stations in China

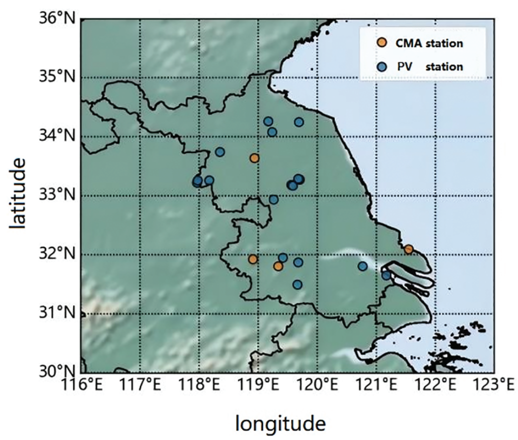

Figure 2: Distribution of surface solar observation stations in Jiangsu Province

To ensure consistency among datasets with different native temporal resolutions, a unified alignment strategy was applied. FY-4A AGRI provides full-disk observations every 15 min, and the Jiangsu PV-site measurements are also recorded at 15-min intervals. In contrast, the CMA observations report instantaneous irradiance values at hourly resolution. Because both CMA and Jiangsu measurements represent instantaneous rather than integrated irradiance, temporal alignment was performed by matching all data sources to the nearest full-hour timestamp. Specifically, the 15-min Jiangsu records were downsampled by selecting the instantaneous measurements at each exact hour, and the FY-4A images corresponding to the same timestamps were extracted. This procedure ensures that all three datasets are temporally synchronized at a 1-h resolution without requiring temporal averaging or interpolation, thereby avoiding potential smoothing of short-term irradiance variability.

2.2 Forecasting Method

XGBoost is a novel algorithm proposed by Chen and Guestrin in 2016 [19,25]. However, unlike the bagging strategy adopted in Random Forest for model training and error correction, XGBoost employs a gradient boosting framework, where trees are built sequentially and each new tree focuses on minimizing the residual errors of the previous ones [26]. XGBoost implements an additive model based on several classification and regression trees (CART). Each new decision tree is added as a base learner to fit the residuals of the previous prediction. The predictions of all decision trees are then accumulated to obtain the final prediction model result. The XGBoost objective function consists of a loss function and a regularization term. This improves upon the gradient boosting decision tree (GBDT) model by using a second-order Taylor expansion of the loss function and introducing first- and second-order derivatives. This effectively controls model overfitting and improves prediction accuracy.

The optimization objective of XGBoost consists of two parts: a loss function for prediction error and a regularization term for model complexity. The overall objective function is defined as:

$$\mathcal{L}(\phi) = \sum_{i=1}^{n} l(y_i, \hat{y}_i) + \sum_{k=1}^{K} \Omega(f_k), \tag{1}$$

where $l(y_i, \hat{y}_i)$ is the loss function of the sample, $\Omega(f_k)$ is the regularization term of the k-th tree, which is used to prevent overfitting.

$$\Omega(f_k) = \gamma T + \frac{1}{2}\lambda \sum_{j=1}^{T} w_j^2, \tag{2}$$

where T is the number of leaf nodes, W_j is the weight of the j-th leaf, γ is the leaf node penalty term, and λ is the L2 regularization coefficient. The regularization term controls the generalization ability of the model by penalizing the complexity of the tree.

At the t-th iteration, the model's predicted value is updated as:

$$\hat{y}_i^{(t)} = \hat{y}_i^{(t-1)} + f_t(x_i), \tag{3}$$

because the loss function $l(y_i, \hat{y}_i)$ is usually nonlinear, XGBoost uses a second-order Taylor expansion around $\hat{y}_i^{(t-1)}$ to approximate it:

$$l\left(y_i, \hat{y}_i^{(t-1)} + f_t(x_i)\right) \approx l\left(y_i, \hat{y}_i^{(t-1)}\right) + g_i f_t(x_i) + \frac{1}{2} h_i f_t(x_i)^2, \tag{4}$$

where $g_i = \frac{\partial l\left(y_i, \hat{y}_i^{(t-1)}\right)}{\partial \hat{y}_i^{(t-1)}}$ represents the first-order derivative of the loss function, $h_i = \frac{\partial^2 l\left(y_i, \hat{y}_i^{(t-1)}\right)}{\partial\left(\hat{y}_i^{(t-1)}\right)^2}$ represents the second-order derivative of the loss function. Setting the derivative with respect to w_j to zero gives the optimal leaf weight:

$$w_j^* = -\frac{G_j}{H_j + \lambda}, \tag{5}$$

and the corresponding optimal objective value of XGBoost is as follows:

$$\mathrm{L}^{(t)} = -\frac{1}{2}\sum_{j=1}^{T} \frac{G_j^2}{H_j + \lambda} + \gamma T, \tag{6}$$

in this study, the constructed XGBoost model integrates 18 features. Among the 14 AGRI spectral bands, 13 were selected as predictors, and were combined with NDVI, two observation angle parameters (including solar zenith angle), elevation, and land-cover information.

2.3 Evaluation Method

Using ground observation station data from Jiangsu Province as the benchmark, corresponding temporal and spatial prediction data were employed for validation. The consistency between daily predicted values and measured values at each station was assessed to evaluate the spatial generalization capability and temporal stability of the XGBoost model in Jiangsu. Evaluation metrics included: Root Mean Square Error (*RMSE*) [27], Mean Absolute Error (*MAE*) [28], *Bias* [29], and Correlation Coefficient (*R*) [30]. The specific formulas are as follows:

$$X_{RMSE} = \sqrt{\frac{1}{n}\sum_{i=1}^{n}\left(F_i - S_i\right)^2}, \tag{7}$$

$$X_{MAE} = \frac{1}{n}\sum_{i=1}^{n}\left|F_i - S_i\right|, \tag{8}$$

$$X_{Bias} = \frac{F_i - S_i}{S_i} \times 100\%, \tag{9}$$

$$R = \frac{\sum_{i=1}^{n}\left(F_i - \overline{F}\right)\left(S_i - \overline{S}\right)}{\sqrt{\sum_{i=1}^{n}\left(F_i - \overline{F}\right)^2 \sum_{i=1}^{n}\left(S_i - S\right)^2}}, \tag{10}$$

where F_i is the i-th predicted irradiance data point, S_i is the i-th ground-observed irradiance data point, $\overline{F}$ is the mean of the predicted data, $\overline{S}$ is the mean of the observed data, and n is the sample size.

3 Results Analysis

3.1 Model Forecast Performance Evaluation

The prediction model uses CMA station observations as ground-truth labels. Fig. 3 compares predicted and observed surface shortwave radiation. The first row presents validation results on the training period, and the second row shows validation results on the testing period. Forecast lead times from left to right are 1, 2, 3, and 4 h.

To avoid temporal information leakage, a chronological split was applied rather than random sampling: the first 80% of the time series at each station was used for model training, and the remaining 20% (the most recent period) for testing. This ensures that the test data strictly postdate the training data, consistent with real forecasting conditions.

The scatter plots show that prediction errors were comparable between the training and testing sets. The root mean square error (RMSE) for the training set ranged from 158.56 to 191.19 W/m^2, while that for the test set ranged from 165.62 to 199.06 W/m^2. The corresponding correlation coefficients ranged from 0.76–0.84 (training) and 0.74–0.82 (test), indicating that the model exhibited neither overfitting nor underfitting. In addition, the feature-importance scores calculated by the XGBoost gain metric show that visible and near-infrared AGRI bands, solar zenith angle, NDVI, and land-cover type contribute most to reducing the prediction error. Features with lower importance are automatically given small weights by the model, and sensitivity tests confirm that removing the least important features only causes a minor RMSE increase. Therefore, retaining all 18 features provides a more robust model under different meteorological conditions.

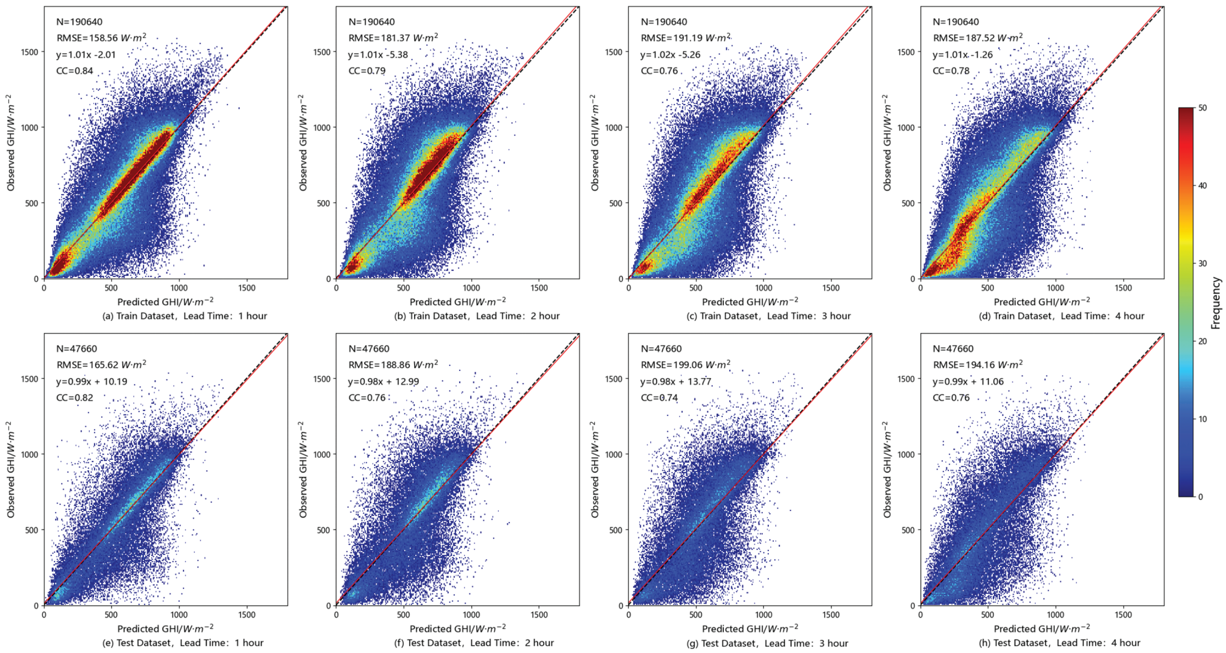

Figure 3: Prediction error testing, with dimensions including testing, training, and forecast duration

3.2 Verification of Forecast Performance within Jiangsu Province

3.2.1 Evaluation of Year-Round Forecast Performance in Jiangsu Province

A total of 17 stations within Jiangsu Province were used for testing, distributed as described in Section 4. Stations 1–3 exhibited significantly different error distributions compared to the others. Among the remaining 14 stations, comprising 21,985 samples, the forecast error testing results are shown in Fig. 4. The root mean square errors for forecast durations ranging from 1 to 4 h were 185.68, 206.20, 211.37, and 200.66 W/m^2, respectively. The RMSE results differ slightly from those obtained using training and testing data. Within Jiangsu Province, the RMSE values increase in the following order: 1, 4, 2, and 3 h. The correlation coefficients were 0.79, 0.74, 0.72, and 0.73, respectively, with the forecast durations ranked from highest to lowest as 1, 2, 4, and 3 h. Overall, the forecast errors for the entire year of 2023 within Jiangsu Province were consistent with the national forecast error distribution.

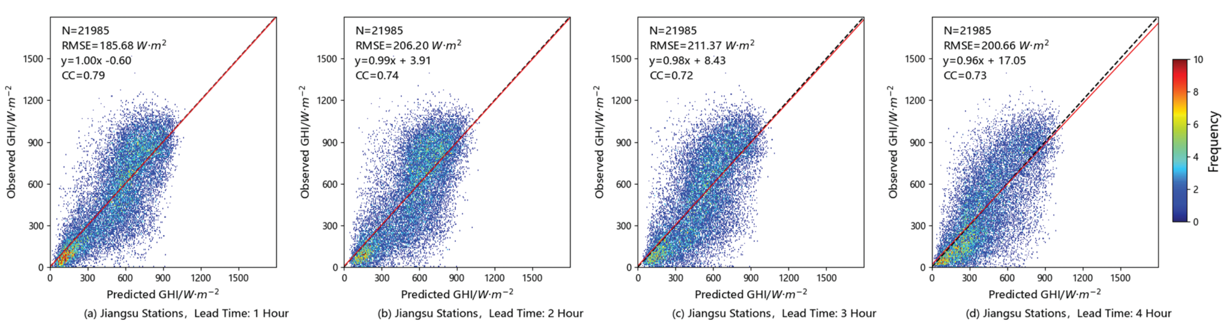

Figure 4: Prediction errors of stations in Jiangsu Province under different forecasts

Stations 1–3 with larger errors were examined individually. Station 1 included 1553 samples, with forecast errors shown in Fig. 5. The root mean square errors for forecast durations of 1 to 4 h were 517.29, 517.39, 493.05, and 440.27 W/m^2, respectively, with correlation coefficients of 0.85, 0.79, 0.77, and 0.78. It can be observed that the station's own GHI observations are consistently within the range of 0–200 W/m^2, whereas GHI observations from stations nationwide or the aforementioned 15 stations within Jiangsu Province fluctuate between 0 and 1400 W/m^2, indicating significant variation. This disparity accounts for the relatively high root mean square error at this station. However, the correlation coefficient for this station is very high. Judging from the correlation coefficient, the model's forecasting performance at this station is superior to that at the 15 stations in Jiangsu Province, indicating that the forecast results are consistent with the observed trend.

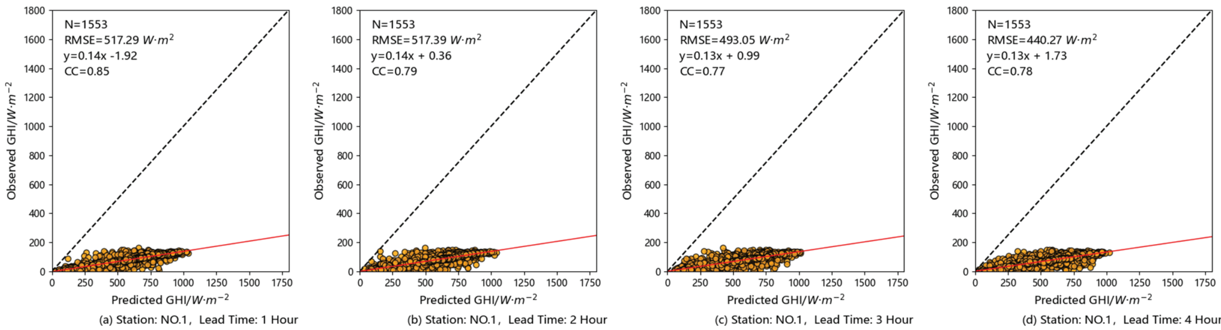

Figure 5: Prediction error of Station 1 in Jiangsu Province under different forecasts

Additionally, Station 2 comprises 1576 samples, with forecast errors shown in Fig. 6. The root mean square errors for forecast durations of 1 to 4 h were 297.59, 303.76, 297.29, and 260.29 W/m^2, respectively, with correlation coefficients of 0.82, 0.77, 0.73, and 0.74. The observed GHI at this station ranged between 0–600 W/m^2, exhibiting issues similar to Station 1. The skewness of its observed GHI relative to other stations contributed to the larger root mean square error at this location. The correlation coefficient between Station 2's forecast results and observed GHI was also high, indicating that the model's forecast trends at Station 2 aligned with observed GHI variations.

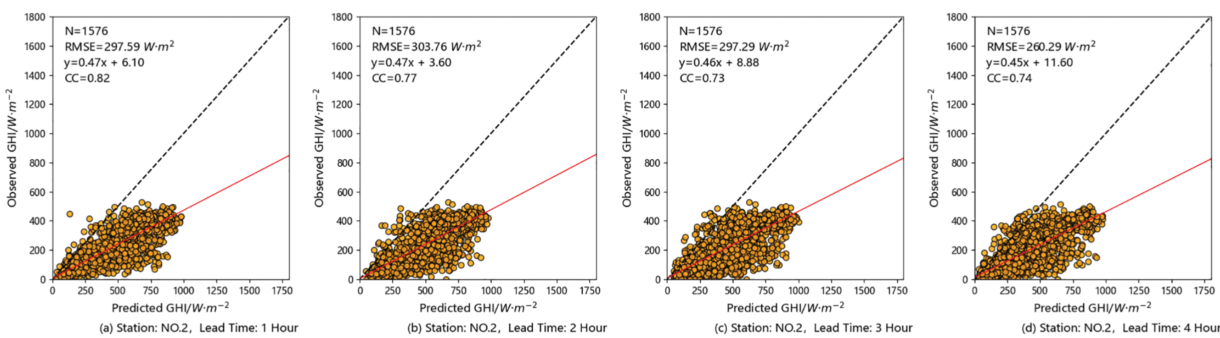

Figure 6: Prediction error of Station 2 in Jiangsu Province under different forecasts

Station 3 comprises 1588 samples, with forecast errors shown in Fig. 7. The root mean square errors for forecast durations of 1 to 4 h were 324.29, 319.18, 308.33, and 269.98 W/m^2, respectively, with correlation coefficients of 0.70, 0.67, 0.68, and 0.72. The observed GHI at this station ranged between 0–1600 W/m^2, differing from Stations 1 and 2. Its relatively higher observed GHI compared to other stations contributed to the larger root mean square error at this location. The correlation coefficient between Station 3's forecast results and observed GHI was also high, indicating that the model's forecast trends at Station 3 aligned with the corresponding observed GHI variations.

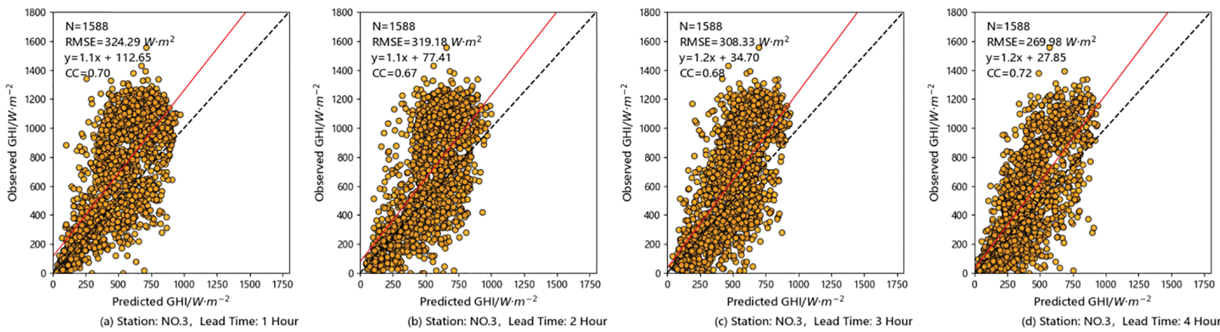

Figure 7: Prediction error of Station 3 in Jiangsu Province under different forecasts

3.2.2 Forecasting Performance across Seasons

Among the 14 stations in Jiangsu Province, the four seasons (spring, summer, autumn, winter) contained 3131, 6146, 7656, and 5052 samples, respectively. The error verification of the forecast results is shown in Fig. 8. The mean root mean square errors for the four seasons were 182.76, 184.86, 223.58, and 194.07 W/m^2. Spring showed the best forecasting performance, followed by summer and winter, while autumn exhibited the largest errors. The scatter plot indicates that during autumn, when GHI values were low, the model tended to overestimate the forecast values. The mean correlation coefficients for the four seasons were 0.81, 0.80, 0.69, and 0.75, respectively, again with spring demonstrating the best forecasting performance, followed by summer and winter, while autumn showed the largest errors.

In the Station 1 dataset, the four seasons comprise 211, 439, 547, and 356 samples, respectively. The error verification of forecast results is shown in Fig. 9. The mean root mean square errors for the four seasons are 396.95, 547.44, 502.04, and 453.53 W/m^2, respectively. Unlike the other 15 stations, Station 1 showed the poorest forecast performance in summer, with autumn and winter exhibiting smaller errors than summer, while spring demonstrated the best forecast results. The mean correlation coefficients for the four seasons were 0.89, 0.82, 0.69, and 0.82, respectively. Autumn showed the poorest forecasting performance, followed by summer and winter, while spring exhibited the highest correlation coefficient. It should be noted that the unusually large RMSE values at Station 1 do not indicate model failure. The observed GHI at this site remains almost entirely within 0–200 W/m^2, which is significantly lower than the typical 0–1400 W/m^2 range observed at other stations. Such a compressed dynamic range causes RMSE to become highly sensitive to even small absolute deviations, mathematically inflating the RMSE although the prediction trend is well reproduced, as reflected by the consistently high correlation coefficients (0.82–0.89). Therefore, the large RMSE arises mainly from the characteristics of the station's measurements rather than from deficiencies in the forecasting model, and RMSE should be interpreted with caution for this particular site.

The samples for Station 2 comprised 229, 434, 547, and 356 cases for spring, summer, autumn, and winter, respectively. The error verification of the forecast results is shown in Fig. 10. The mean root mean square errors for the four seasons were 173.49, 304.36, 333.39, and 258.13 W/m^2, respectively. Among Station 2's forecast results, autumn showed the poorest prediction performance, while summer and winter errors were smaller than those in autumn. Spring demonstrated the best forecast effectiveness. The mean correlation coefficients for the four seasons were 0.88, 0.84, 0.73, and 0.81, respectively. Spring showed the best forecasting performance, followed by summer and winter, while autumn had the lowest correlation coefficient.

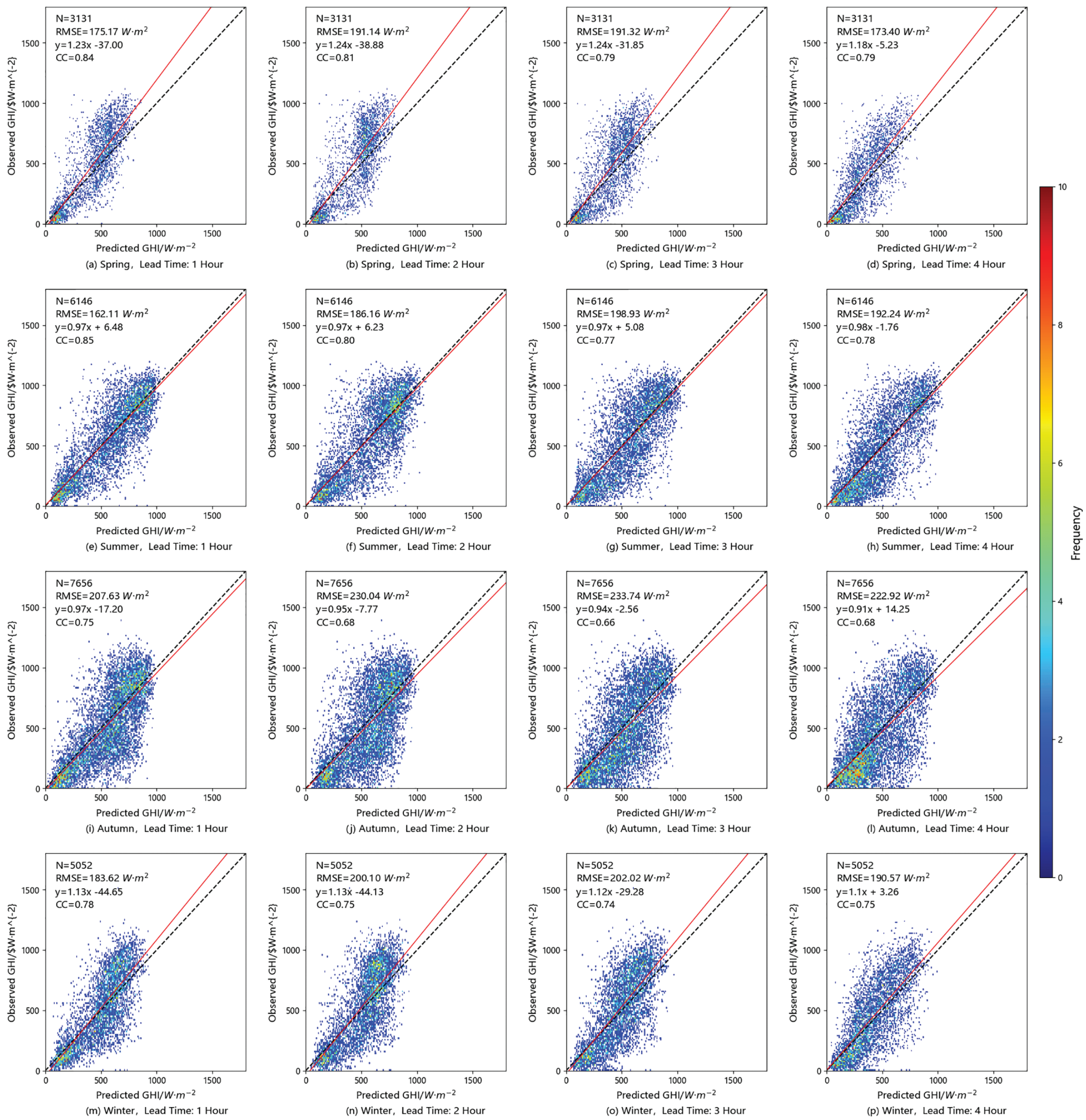

Figure 8: Prediction error of stations in Jiangsu Province under different forecasts

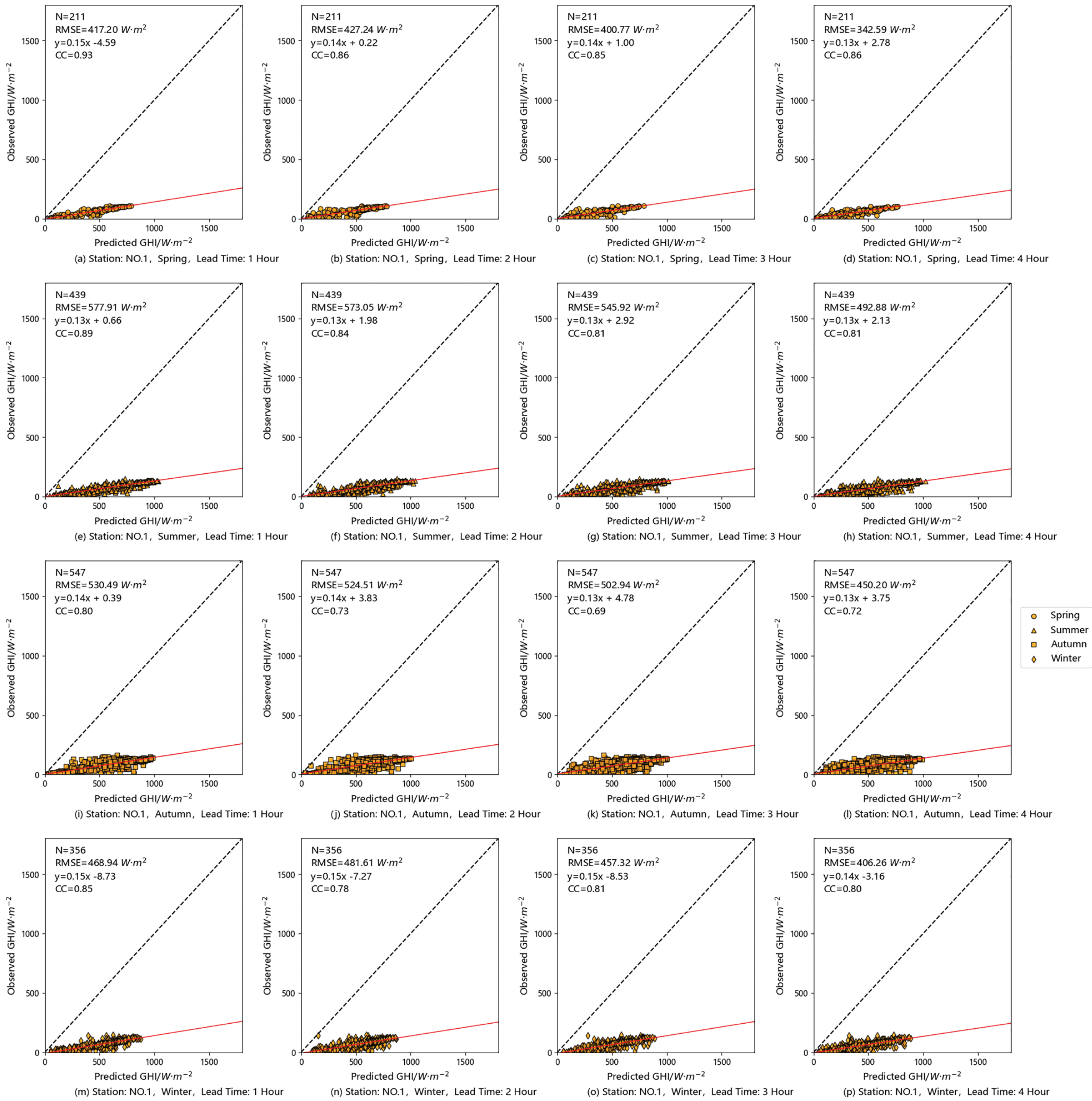

Figure 9: Prediction error of Station 1 in Jiangsu Province under different forecasts

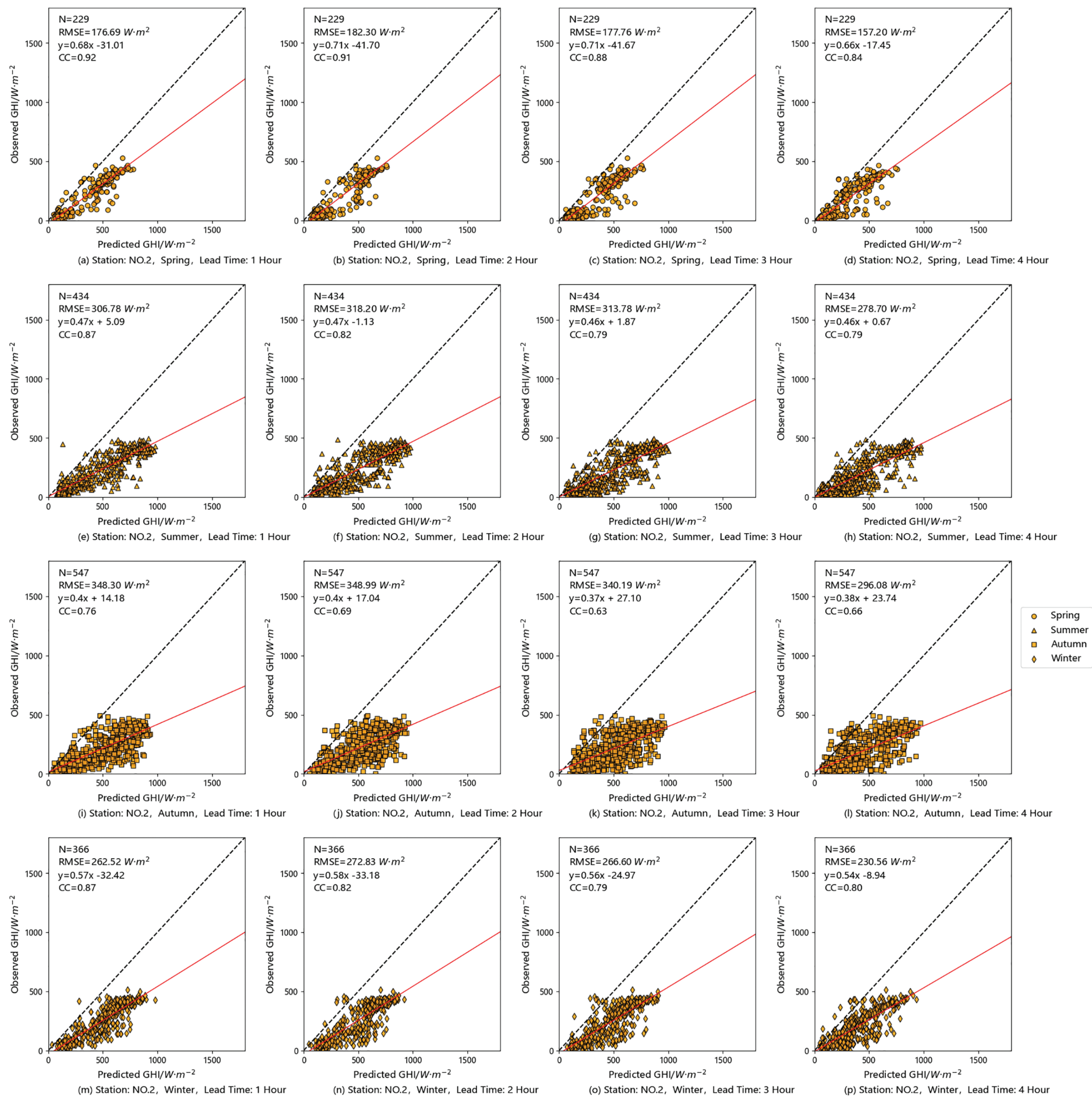

Figure 10: Prediction error of station 2 in Jiangsu Province under different forecasts

The station 3 dataset comprises 226, 447, 551, and 364 samples for spring, summer, autumn, and winter, respectively. The prediction error validation results are shown in Fig. 11. The mean root mean square errors for the four seasons were 425.33, 235.60, 264.24, and 346.85 W/m^2, respectively. Among Station 3's forecast results, spring showed the poorest prediction performance, while winter and autumn exhibited smaller errors than summer. Spring demonstrated the best forecasting effectiveness. The mean correlation coefficients for the four seasons were 0.85, 0.77, 0.70, and 0.80, respectively. Spring showed the best forecasting performance, followed by summer and winter, while autumn had the lowest correlation coefficient. Regarding forecast performance within Jiangsu Province, the root mean square error (RMSE) holds a limited reference value for Sites 1–3 due to differences in the absolute magnitude of observed values compared to training sample values. However, the correlation coefficients for Sites 1–3 indicate that the model's forecast performance is best in spring and worst in autumn across these three sites. This suggests that autumn weather patterns may be more complex, leading to larger errors.

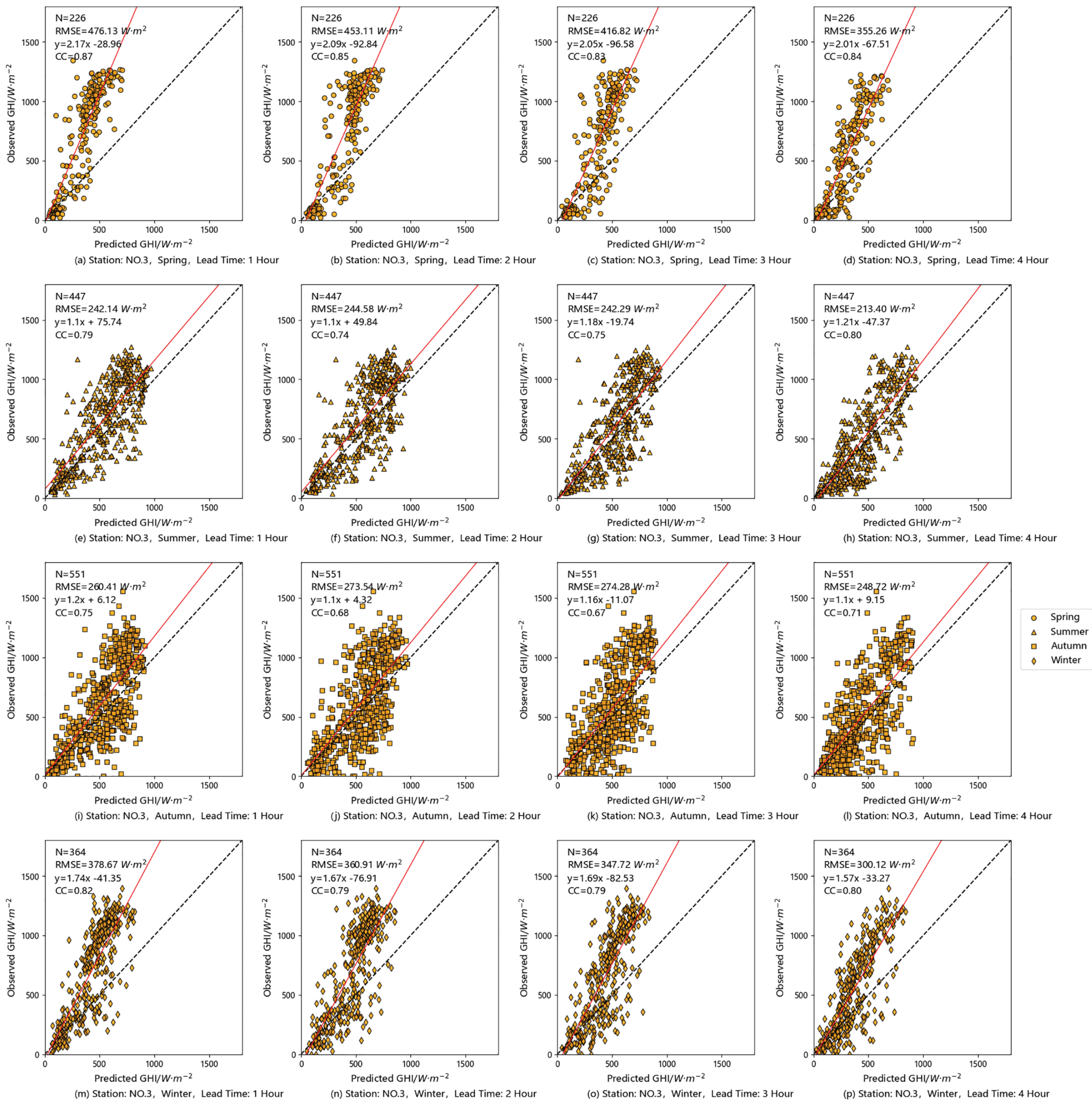

Figure 11: Prediction error of station 3 in Jiangsu Province under different forecasts

3.2.3 Statistical Analysis of Forecast Performance across Stations

Statistics on the forecasting performance of 17 stations in Jiangsu Province for the entire year of 2023 are presented in Table 1, showing the root mean square error (RMSE) and correlation coefficients for each station. It can be observed that, except for Stations 1–3 which exhibit significant systematic biases resulting in larger RMSE values, the 1-h forecast RMSE for all other stations is less than 215 W/m^2, and the 2–4 h forecast RMSE was less than 265 215 W/m^2. For all 17 stations, the correlation coefficients for 1-h and 2-h forecasts exceeded 0.70, while those for 2-h and 3-h forecasts exceeded 0.65.

Table 1: Error statistics of annual forecast results in Jiangsu Province (17 stations in total)

Station	Samples	RMSE (W/m^2)				CC			
		1-h	2-h	3-h	4-h	1-h	2-h	3-h	4-h
1	1553	517.29	517.39	493.05	440.27	0.85	0.79	0.77	0.78
2	1576	297.59	303.76	297.29	260.29	0.82	0.77	0.73	0.74
3	1588	324.29	319.18	308.33	269.98	0.70	0.67	0.68	0.72
4	1574	214.53	242.44	253.28	238.84	0.81	0.75	0.74	0.76
5	1572	146.14	168.46	180.76	175.71	0.84	0.78	0.75	0.76
6	1571	175.40	201.01	210.75	208.02	0.80	0.73	0.71	0.71
7	1572	188.87	203.20	208.90	196.25	0.76	0.72	0.71	0.74
8	1569	206.36	212.33	208.52	196.24	0.83	0.79	0.76	0.76
9	1587	179.49	210.01	223.30	224.17	0.81	0.74	0.72	0.73
10	1565	214.51	221.83	208.58	180.89	0.79	0.75	0.75	0.78
11	1568	200.46	226.88	232.79	220.14	0.82	0.76	0.74	0.76
12	1567	201.89	211.82	207.04	187.80	0.77	0.72	0.72	0.75
13	1585	155.05	177.81	180.65	172.15	0.83	0.76	0.76	0.78
14	1574	160.39	180.27	187.00	181.76	0.83	0.78	0.74	0.75
15	1550	210.09	240.81	250.57	231.56	0.80	0.73	0.70	0.74
16	1555	169.16	192.00	201.03	197.47	0.83	0.78	0.76	0.77
17	1576	157.75	181.73	190.27	183.36	0.84	0.78	0.75	0.76

3.2.4 Sequential Comparison of Station Forecast Results

To evaluate the model's continuous forecasting performance, Stations 13 and 16 were selected for two-day validation on 1 June and 1 September. The forecast results for Station 13 are shown in Fig. 12. On 1 June, the sky was fully overcast and the observed GHI remained close to zero throughout most of the day. Under such conditions, the diurnal radiation cycle becomes indistinguishable, and both the observed and predicted curves appear nearly flat. This visual flatness may give the impression that the model predicts only "half of a day", whereas the model in fact produced full-day forecasts. The lack of visible structure is due to the extremely low radiation environment rather than a limitation of the model.

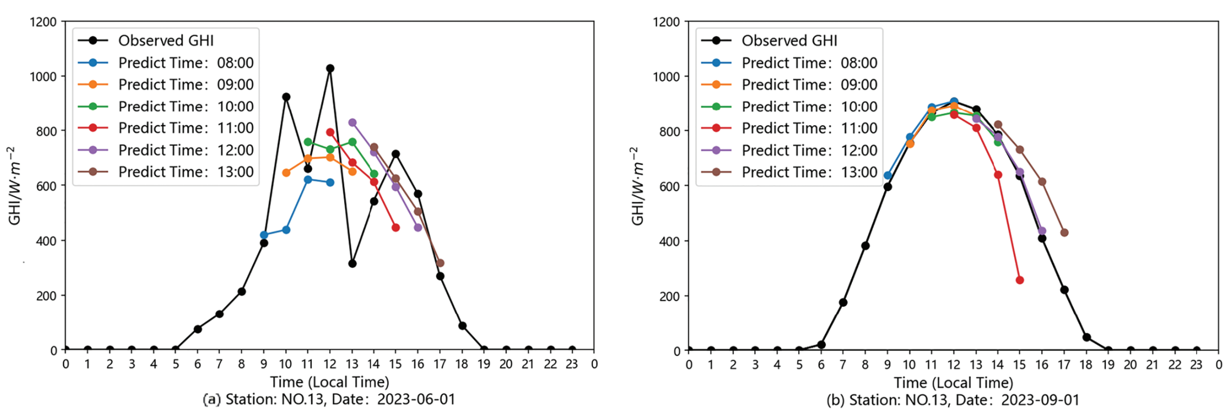

Figure 12: Verification of forecast results for Site 13 under different weather conditions

In contrast, under clear-sky conditions on 1 September (Fig. 12b), the model accurately captured the complete diurnal cycle, including peak irradiance and inflection points. This demonstrates its capability for operational photovoltaic forecasting when meaningful radiation signals are present.

The forecast performance for Station 16 is shown in Fig. 13. Similarly, although radiation on 1 June was extremely low, the weather conditions resulted in discrepancies between forecast and observed values. However, the model still captured the correct direction of rapid irradiance transitions between 11:00 and 12:00. Under clear skies on 1 September, the forecasts closely matched the observations, showing consistent trends and accurately predicting the inflection point of the GHI curve.

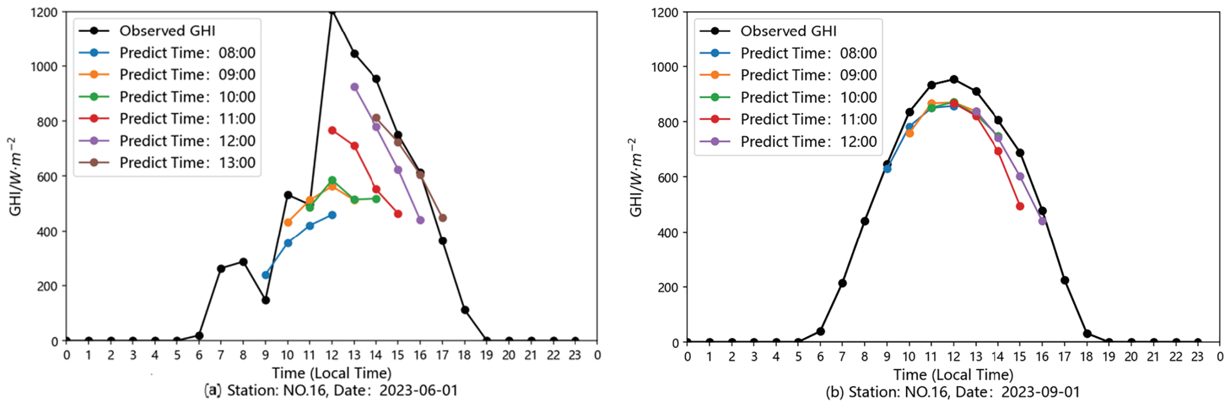

Figure 13: Verification of forecast results for Site 16 under different weather conditions

Although Fig. 12a exhibits minimal fluctuations, it remains meaningful because it represents a common cloudy-day scenario in which suppressed irradiance is physically correct. Flat predicted values under such weather conditions reflect appropriate model behavior rather than model failure. Furthermore, we clarify that the operational forecasting window of this study is 09:00–17:00, which aligns with both FY-4A visible-band data availability and the key period for photovoltaic power generation. The proposed method provides 0–4-h forecasts within this window, and improving performance under transition-type weather (such as that shown in Fig. 12a) will be a focus of future work.

3.2.5 Error Attribution for High-RMSE Sites (Sites 1–3)

To elucidate the mechanisms responsible for the large forecast errors observed at Sites 1–3, the relationships between model residuals and key atmospheric and surface parameters were systematically examined. The analysis focused on three dominant factors that directly modulate shortwave radiation reaching the surface: aerosol optical depth (AOD), low-cloud frequency, and surface albedo associated with land-cover heterogeneity. Hourly AOD values were retrieved from FY-4A AGRI data following an established inversion algorithm, while low-cloud occurrence was quantified using cloud optical thickness (COT) retrieved from daytime FY-4A observations. Surface albedo and land-cover information were extracted from the same geospatial dataset used in the model's feature set. These diagnostics were compared with site-level forecast errors across all seasons to identify persistent patterns and determine whether local atmospheric and surface conditions systematically influenced prediction performance.

At Site 1, the observed ground horizontal irradiance (GHI) remains largely within 0–200 W/m^2, indicating a limited dynamic range compared with the model's training distribution. This anomaly is consistent with potential issues in the local measurement system, such as sensor calibration, mounting configuration, or partial shading. In addition, persistent high AOD values and frequent low-cloud events during spring and autumn jointly enhance shortwave radiation attenuation over coastal and heterogeneous underlying surfaces. Consequently, the model exhibits relatively large RMSEs despite maintaining high correlation coefficients between predictions and observations. This indicates that magnitude bias—linked to both local observational characteristics and complex radiative conditions—rather than random error dominates at this site.

At Site 2, the GHI distribution (0–600 W/m^2) is narrower and more asymmetric than that of other stations in Jiangsu Province. The seasonal rise in low-cloud frequency during transitional months, together with moderate aerosol loading, coincides with higher forecast errors. The surrounding urbanized landscape contributes additional subpixel-scale heterogeneity, weakening the accuracy of FY-4A retrievals and leading to a degradation in predictive performance. This behavior underscores the influence of urban surface complexity and its interaction with partially cloudy conditions as a limiting factor in short-term solar irradiance forecasts.

Site 3 demonstrates a much broader GHI range, extending up to approximately 1600 W/m^2, yet still shows substantial forecast errors. Elevated aerosol loading and rapidly varying low-level clouds are common in this region and generate large short-term fluctuations in atmospheric transmissivity. The model tends to underestimate these changes at forecast lead times of 2–4 h, reflecting its limited sensitivity to mesoscale variability and aerosol–cloud coupling processes. These results highlight the importance of incorporating dynamic aerosol and cloud features to capture transient radiative effects more effectively.

Overall, the diagnostic analysis reveals that the large RMSEs at the three anomalous sites primarily stem from the combined influence of elevated aerosol optical depth, frequent low-cloud occurrence, and complex coastal or urban surface heterogeneity. These local atmospheric and surface factors amplify radiation attenuation and induce forecast uncertainty. Implementing targeted data-quality control measures—such as automated detection of instrument shading—and applying site-specific bias correction schemes are expected to further mitigate these errors and enhance model robustness across diverse surface environments.

In addition, the Jiangsu stations are operated within photovoltaic power plants rather than within the national CMA radiation network. The associated irradiance sensors may differ from CMA instruments in terms of model, calibration protocol, mounting height and tilt, and exposure to partial shading or soiling from nearby PV structures. Although grossly erroneous records were removed through our quality-control procedure, a certain level of residual observational uncertainty at these PV sites cannot be completely excluded and may also contribute to the larger RMSE values reported for Jiangsu. Nevertheless, the consistently high correlation coefficients ($R > 0.70$ at all 17 stations) indicate that the forecasting model still captures the short-term variability of GHI reliably, and the larger errors should be interpreted mainly as a combination of local environmental complexity and observation-system differences rather than a fundamental limitation of the model.

4 Conclusions

This study utilized FY-4A satellite data from 2023 and GHI observations from CMA stations to establish a short-term (1–4 h) GHI forecast model for China using the XGBoost algorithm. The model was independently validated across 17 stations in Jiangsu Province. The results indicate:

(1) The model's generalization capability was validated. The forecast errors in Jiangsu Province (RMSE 165.62–199.06 W/m^2) closely matched those in the national training dataset (158.56–191.19 W/m^2), confirming the applicability of machine learning models at regional scales. This finding resonates with Wang et al. (2024)'s conclusions from Anhui photovoltaic stations, where their XGBoost model enhanced radiation inversion accuracy by over 5% through integrating FY-4A multispectral

data—further demonstrating geostationary satellite data's predictive advantage for complex surface areas [12].

(2) Forecast results reveal seasonal variation mechanisms, with spring-summer prediction accuracy in Jiangsu Province (RMSE 182–185 W/m^2) significantly outperforming autumn-winter (194–224 W/m^2), consistent with Yan et al.'s findings in Yinchuan [31]. The research team discovered that the synergistic effect of autumn aerosol optical depth (AOD > 1.2) and cloud water path (CWP > 300 g/m^2) leads to enhanced radiation attenuation. In contrast, spring exhibits higher cloud cover (68% coverage) but predominantly features ice clouds, resulting in a 22% higher proportion of penetrating radiation compared to winter and corroborating the simulation results from the cloud-radiation coupling model established by Jia et al. in the Yangtze River Delta region.

(3) The prediction model demonstrates multi-timescale forecasting capability, with 1-h forecast accuracy (R = 0.82) significantly outperforming 4-h forecasts (R = 0.73). Notably, the 3-h forecast period exhibits an error peak (RMSE 211.37 W/m^2), which may be linked to the onset of mesoscale convective systems. Similar temporal patterns were reported by Zhang et al. (2021) and Li et al. (2022), who found that rapid cloud formation during convective transitions causes abrupt GHI drops in East China [32,33].

(4) Anomaly site error tracing indicates that the systematic errors (RMSE > 300 W/m^2) at three anomalous sites likely stem from local observational environment differences. Factors such as surface albedo, proximity to densely built-up areas, or mining zones may contribute to observational discrepancies.

This study confirms the application potential of FY-4A satellite data for short-term irradiance forecasting along China's eastern coast, providing a prediction tool with sub-200 W/m^2 error for regions with high photovoltaic grid integration. Future work may integrate FY-4B, Himawari-8, and ground-based meteorological observations to establish a multi-source collaborative forecasting system with enhanced spatio-temporal resolution.

Acknowledgement: Not applicable.

Funding Statement: This research was funded by State Grid Jiangsu Electric Power Co., Ltd., grant number J2024077.

Author Contributions: The authors confirm contribution to the paper as follows: conceptualization, Yunlong Du and Shuyi Zhuang; methodology, Yunlong Du; software, Zhigang Ye; validation, Qiangsheng Bu, Yun Chai and Yuanbing Wang; formal analysis, Yunlong Du; investigation, Yunlong Du; resources, Yunlong Du; data curation, Yunlong Du; writing—original draft preparation, Shuyi Zhuang; writing—review and editing, Shuyi Zhuang; visualization, Shuyi Zhuang; supervision, Yuanbing Wang; project administration, Yuanbing Wang; funding acquisition, Shuyi Zhuang. All authors reviewed the results and approved the final version of the manuscript.

Availability of Data and Materials: The data that support the findings of this study are available from the Corresponding Author, Shuyi Zhuang, upon reasonable request.

Ethics Approval: Not applicable.

Conflicts of Interest: The authors declare no conflicts of interest to report regarding the present study.

References

1. Yuan Y, Zhai P. Latest understanding of extreme weather and climate events under global warming and urbanization influences. Trans Atmos Sci. 2022;45(2):161–6.
2. Sayeed A, Adil S, Mallah HB. Climate change vulnerabilities in Sindh, Pakistan. Int Growth Cent. 2024:1–43.
3. Fang J, Zhu J, Wang S, Yue C, Shen H. Global warming, human-induced carbon emissions, and their uncertainties. Sci China Earth Sci. 2011;54(10):1458–68. doi:10.1007/s11430-011-4292-0.

4. Zhu X, Gong B. Risk challenges and path options for realizing the dual-carbon goal in the context of high-quality development in China. In: Chinese governance and transformation towards carbon neutrality. Singapore: Springer Nature; 2024. p. 71–89.
5. Mukhoty BP, Maurya V, Shukla SK. Sequence to sequence deep learning models for solar irradiation forecasting. In: Proceedings of the 2019 IEEE Milan PowerTech; 2019 Jun 23–27; Milan, Italy. p. 1–6. doi:10.1109/ptc.2019.8810645.
6. Zeng Z, Wang Z, Gui K, Yan X, Gao M, Luo M, et al. Daily global solar radiation in China estimated from high-density meteorological observations: a random forest model framework. Earth Space Sci. 2020;7(2):1–15. doi:10.1029/2019EA001058.
7. Ellrod GP, Pryor K. Applications of geostationary satellite data to aviation. Pure Appl Geophys. 2019;176(5):2017–43. doi:10.1007/s00024-018-1821-1.
8. Yang J, Zhang Z, Wei C, Lu F, Guo Q. Introducing the new generation of Chinese geostationary weather satellites, Fengyun-4. Bull Am Meteor Soc. 2017;98(8):1637–58. doi:10.1175/bams-d-16-0065.1.
9. Bessho K, Date K, Hayashi M, Ikeda A, Imai T, Inoue H, et al. An introduction to himawari-8/9—Japan's new-generation geostationary meteorological satellites. J Meteorol Soc Jpn. 2016;94(2):151–83. doi:10.2151/jmsj.2016-009.
10. Chung SR, Ahn MH, Han KS, Lee KT, Shin DB. Meteorological products of geo-KOMPSAT 2A (GK2A) satellite. Asia Pac J Atmos Sci. 2020;56(2):185. doi:10.1007/s13143-020-00199-x.
11. Wang L, Shi J. A comprehensive application of machine learning techniques for short-term solar radiation prediction. Appl Sci. 2021;11(13):5808. doi:10.3390/app11135808.
12. Wang F, Li N, Su Y, Sun Y, Yang H, Zhen Z. Spatiotemporal correlation mapping and prediction modeling of irradiance based on satellite remote sensing. Acta Energiae Solaris Sin. 2024;45(3):1–9. (In Chinese).
13. Jia D, Li K, Gao X. Nowcasting prediction of solar irradiance based on FY-4A and machine learning. Acta Energiae Solaris Sin. 2024;45(4):578–83. (In Chinese).
14. Li N, Zhen Z, Wang F. Spatio-temporal correlation-based surface solar irradiance retrieval approach using satellite data under different weather conditions. [cited 2025 Jan 1]. Available from: https://ssrn.com/abstract=4832943.
15. Fu C, Jiang Z, Guan Z, He J, Xu Z. Climate of China and East Asian monsoon. In: Regional climate studies of China. Berlin/Heidelberg, Germany: Springer; 2008. p. 1–48. doi:10.1007/978-3-540-79242-0_1.
16. Zhong S, Qian Y, Zhao C, Leung R, Wang H, Yang B, et al. Urbanization-induced Urban heat Island and aerosol effects on climate extremes in the Yangtze River Delta region of China. Atmos Chem Phys. 2017;17(8):5439–57. doi:10.5194/acp-17-5439-2017.
17. Zhu S, Ma Z. Does FY-4A AGRI capture precipitation motions? IEEE Geosci Remote Sens Lett. 2021;19:1–5.
18. Gao Y, Mao D, Wang X, Qin D. Evaluation of FY-4A temperature profile products and application to winter precipitation type diagnosis in southern China. Remote Sens. 2022;14(10):2363. doi:10.3390/rs14102363.
19. Xu F, Song B, Chen J, Guan R, Zhu R, Liu J, et al. Deep-learning-based daytime COT retrieval and prediction method using FY4A AGRI data. Remote Sens. 2024;16(12):2136. doi:10.3390/rs16122136.
20. Ustin SL, Middleton EM. Current and near-term earth-observing environmental satellites, their missions, characteristics, instruments, and applications. Sensors. 2024;24(11):3488. doi:10.3390/s24113488.
21. Mousivand A, Verhoef W, Menenti M, Gorte B. Modeling top of atmosphere radiance over heterogeneous non-lambertian rugged terrain. Remote Sens. 2015;7(6):8019–44. doi:10.3390/rs70608019.
22. Jiang X, Xue Y, Jin C, Bai R, Sun Y, Wu S. A simple band ratio library (BRL) algorithm for retrieval of hourly aerosol optical depth using FY-4A AGRI geostationary satellite data. Remote Sens. 2022;14(19):4861. doi:10.3390/rs14194861.
23. Liu H, Hu B, Zhang L, Zhao XJ, Shang KZ, Wang YS, et al. Ultraviolet radiation over China: spatial distribution and trends. Renew Sustain Energy Rev. 2017;76:1371–83. doi:10.1016/j.rser.2017.03.102.
24. Shi H, Yang D, Wang W, Fu D, Gao L, Zhang J, et al. First estimation of high-resolution solar photovoltaic resource maps over China with Fengyun-4A satellite and machine learning. Renew Sustain Energy Rev. 2023;184:113549. doi:10.1016/j.rser.2023.113549.

25. Chen T, Guestrin C. XGBoost: a scalable tree boosting system. In: Proceedings of the 22nd ACM SIGKDD International Conference on Knowledge Discovery and Data Mining; 2016 Aug 13–17; San Francisco, CA, USA. New York, NY, USA: ACM; 2016. p. 785–94. doi:10.1145/2939672.2939785.
26. Sahin EK. Assessing the predictive capability of ensemble tree methods for landslide susceptibility mapping using XGBoost, gradient boosting machine, and random forest. SN Appl Sci. 2020;2(7):1308. doi:10.1007/s42452-020-3060-1.
27. Chai T, Draxler RR. Root mean square error (RMSE) or mean absolute error (MAE)?—Arguments against avoiding RMSE in the literature. Geosci Model Dev. 2014;7(3):1247–50. doi:10.5194/gmd-7-1247-2014.
28. Willmott CJ, Matsuura K. Advantages of the mean absolute error (MAE) over the root mean square error (RMSE) in assessing average model performance. Clim Res. 2005;30:79–82. doi:10.3354/cr030079.
29. Delgado-Rodríguez M, Llorca J. Bias. J Epidemiol Commun Health. 2004;58(8):635–41. doi:10.1136/jech.2003.008466.
30. Asuero AG, Sayago A, González AG. The correlation coefficient: an overview. Crit Rev Anal Chem. 2006;36(1):41–59. doi:10.1080/10408340500526766.
31. Yan X, Ye D, Shen Y, Na L, Hu Y, Jiang T. Study on applicability of FY-4A radiation products in short-term solar radiation forecast in Yinchuan. Acta Energiae Solaris Sin. 2025;46(2):511–21. (In Chinese).
32. Zhang X, Shen W, Zhuge X, Yang S, Chen Y, Wang Y, et al. Statistical characteristics of mesoscale convective systems initiated over the Tibetan Plateau in summer by Fengyun satellite and precipitation estimates. Remote Sens. 2021;13(9):1652. doi:10.3390/rs13091652.
33. Li J, Jiang Y, Xia X, Hu Y. Increase of surface solar irradiance across East China related to changes in aerosol properties during the past decade. Environ Res Lett. 2018;13(3):034006. doi:10.1088/1748-9326/aaa35a.